Monitoring shallow geothermal aquifers with active-source Distributed Acoustic Sensing: a prognostic feasibility study on the University of Leeds Geothermal Campus

Adam D. Booth[1], Roger A. Clark[1], Andy Nowacki[1], Ravi Myanger[1,2], Joseph Kelly[1,3], Sjoerd de Ridder[1], Arka Dyuti Sarkar[1,4], Fleur Loveridge[3], Richard Collier[1], Emma Bramham[1] and David Healy[5].

1. School of Earth, Environment and Sustainability, University of Leeds, Leeds, LS2 9JT, United Kingdom

2. Now at: DUG Technology, 3rd Floor, 192-198 Vauxhall Bridge Road, London, SW1V 1DX, United Kingdom

3. School of Civil Engineering, University of Leeds, Leeds, LS2 9JT, United Kingdom

4. Now at: School of Natural and Built Environment, Queen's University Belfast, University Road, Belfast, BT7 1NN, United Kingdom

5. Geosolutions Leeds, School of Earth, Environment and Sustainability, University of Leeds, Leeds, LS2 9JT, United Kingdom

Corresponding author: Adam Booth (a.d.booth@leeds.ac.uk)

ABSTRACT

The UK's shallow aquifers offer significant but underdeveloped geothermal energy resource. Seismic methods can help address this, by improving the understanding of aquifer heterogeneity and potentially allowing long-term monitoring of thermal plumes. Here, we consider the derivation of seismic velocity and attenuation models from borehole distributed acoustic sensing (DAS) data, recorded on the University of Leeds Geothermal Campus. We record active-source seismic shots in a 250 m-long vertical cable, that samples two fractured sandstone aquifers (Elland Flags and Rough Rock). Compressional wave velocities (v_P) are obtained to 160 m depth, and are typically 3100 ± 50 m s^{-1} through the Elland Flags. To predict the value of v_P for thermal monitoring, we simulate groundwater warming in a Hashin-Shtrikman petrophysical framework, which suggests that ±50 m s^{-1} precision is sufficient to detect heating > 26 °C (> 14 °C above ambient temperature). Although this is at the upper range of likely temperature change in a shallow geothermal system under typical usage, UK environmental legislation restricts heating to

< 25 °C therefore our approach could be used to support the monitoring of operational compliance. Refining both the DAS acquisition and measurement of seismic quantities (v_P and quality factor) should improve precision and thus facilitate monitoring of more subtle heating expressions.

Keywords: Distributed Acoustic Sensing, Vertical Seismic Profile, geothermal aquifer, petrophysics, seismic velocity, quality factor

1. Introduction

Heating accounts for around half of global energy demand, with 75% of that supplied by fossil fuels (European Commission, 2016). In the UK, heating buildings is responsible for ~25% of carbon emissions (Climate Change Commission, 2020) with gas-fired heating systems being widespread in domestic buildings. Decarbonising the supply of electricity has been relatively straightforward because the interventions required (e.g., renewable energy sources including wind and solar) require little retrofitting at the point of use to implement and therefore are relatively unimpactful on public life. Retrofitting UK heating/cooling systems is a much more significant challenge: reducing carbon emissions would require intervention in almost every UK building. Technologies that both achieve net zero goals and minimise disruption are therefore attractive, and UK geothermal energy can have a significant role to play in future energy provision. Many UK urban centres are underlain by shallow geothermal reservoirs, offering storage and extraction options for excess heat and providing significant reductions in carbon demand (Abesser et al., 2020). Nevertheless, the UK has been slow to explore geothermal heating solutions, owing to i) lack of knowledge about the geological and hydrological complexity of geothermal reservoirs, and ii) stakeholder concerns about the long-term sustainability, and thus cost-effectiveness, of geothermal heating. These obstacles are clearly intertwined, and in demonstrating improved understanding of the subsurface controls on a geothermal system, there is greater likelihood of stakeholder investment.

Geophysical intelligence therefore has a significant role to play in advancing the uptake of geothermal technologies. From initial resource identification, through stages of system

design and ultimately monitoring the sustainability of the geothermal facility and ensuring compliance with environmental legislation, geophysics is (or could be) a major component of developing a geothermal resource. Often, a major stakeholder concern relates to the risk of induced seismicity, hence seismic monitoring can be undertaken around prospective sites (e.g., Zang et al., 2014; Koirala et al., 2024). Since geothermal developments included purpose-drilled boreholes, technologies that are compatible with borehole deployments are also attractive: these include fibre optic cables for distributed temperature sensing (DTS) and distributed acoustic sensing (DAS). Several studies document the application of DTS across a range of geothermal depth scales (e.g., Liu et al., 2023; Kyrkou et al., 2026; Seib et al., 2025) but DAS methods, where they are applied, support measurements of seismicity in deep and/or engineered geothermal systems (Azzola et al., 2023; Chamarczuk et al., 2025).

The application of DAS to shallow and/or low enthalpy geothermal systems is less developed although numerous test-sites in the UK recognise its potential and contain DAS capabilities (e.g., the British Geological Survey's UK Geoenergy Observatories; Holmgren et al., 2025). Carpentier et al. (2020) show applications of DAS for characterising the structure of a shallow geothermal site, but there has been limited assessment of whether DAS technologies are compatible with the direct detection of thermal change via seismic velocity and attenuation. For characterising heat specifically, DTS technologies (e.g., Iten et al., 2024; Kyrkou et al., 2026) clearly provide the most direct assessment of the thermal state of an aquifer. However, DTS insight is limited to the immediate vicinity of the borehole. By contrast, through time-lapse imaging with either active- or passive-source approaches, DAS could extend sensitivity into the reservoir: with a reliable link between temperature and seismic properties (e.g., velocity or attenuation) and sufficient sensitivity, DAS could be valuably applied to tracking the evolution and interference of thermal plumes. DAS monitoring could also help ensure that geothermal operations comply with local environmental permitting. In the UK, for example, a licence is required for abstraction and reinjection of groundwater which typically stipulates injection temperature limits to prevent adverse impacts on ground- and surface-water ecosystems; in practice, this commonly prevents any geothermal development from increasing groundwater temperature above 25°C, or ~10°C above existing ambient temperature (Environment Agency, n.d.).

In this paper, we assess the feasibility of detecting thermal change under plausible heating scenarios in a shallow ground-source heating/cooling system, using active-source DAS to estimate compressional (P-) wave velocity (v_P) and quality factor (Q_P). DAS recordings were undertaken on the University of Leeds (UoL) campus, in one of several appraisal boreholes that were drilled to explore geothermal solutions to energy provision. Data were recorded opportunistically while checking the variability of cable coupling in the borehole, preceding a forthcoming programme of thermal testing, and providing a baseline dataset to benchmark any seismic expression of hot- or cold- water injection. We first review the borehole infrastructure on the UoL campus and the aquifers it targets, before assessing velocity models derived from DAS vertical seismic profiles (VSPs) for their sensitivity to groundwater temperature change. In so doing, we evaluate the use of DAS methods both for monitoring the sustainability of a geothermal system under production and as a potential means, cost notwithstanding, of ensuring that a geothermal development complies with legislative frameworks.

2. Site overview: target geology and borehole infrastructure

2.1 University of Leeds' Geothermal Campus

The UoL Climate Plan commits the university to achieving net-zero carbon emissions by 2030. As part of this initiative, and to provide a 'living lab' for exploring geothermal heating/cooling systems more widely, UoL constructed eleven boreholes at targeted locations around its campus (Figure 1). With reference to acronyms for the nine boreholes shown in Figure 1,

- four closed-loop (CL) boreholes, allowing water circulation within HDPE (high-density polyethylene) U-loops and thermal response testing (TRT) (Claesson and Eskilson, 1988; Loveridge et al., 2013),
- two open-loop (OL) boreholes, in which hot or cold water can be injected, extracted and circulated through target aquifers, and
- three pilot wells (PW), which are cored and logged with wireline tools, and kept open (in part, with slotted casing) to allow further geophysical / hydrological monitoring.

All boreholes include single-mode fibre optic cables, appropriate for Rayleigh and Brillouin backscatter analysis, and include both loose- and tight-buffered fibres (to differentiate strain and temperature effects when using Brillouin interrogators; Sparrevik et al., 2022). The cable

is most often grouted between the borehole casing and the borehole wall but is held in permeable shingle in intervals where water ingress into boreholes is desirable. The cables have a single-ended installation: there is no return leg from the base of the borehole, and the cable end is terminated with a rubber heat-shrink cap to minimise water ingress.

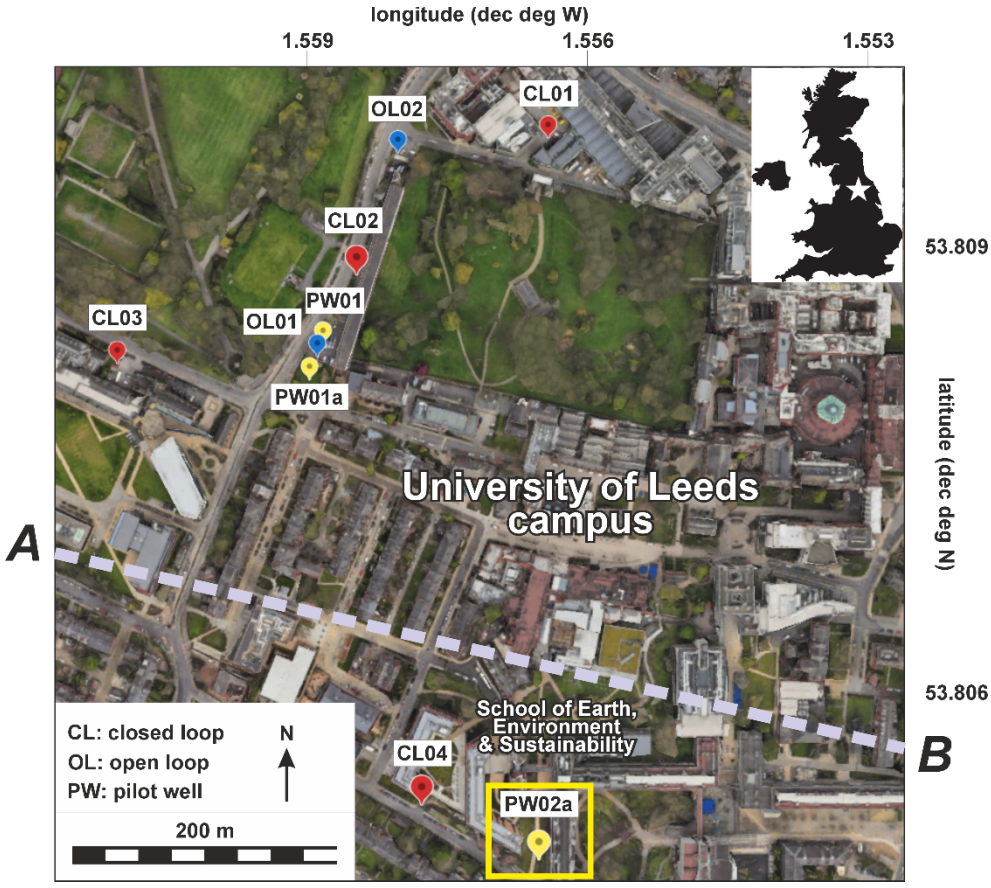

Figure 1: University of Leeds campus map and the location of geothermal boreholes. The most southerly borehole, PW02a, is the primary focus of this paper. Aerial imagery from Google Earth, featuring data from Data SIO, NOAA, U.S. Navy, NGA, GEBCOLandsat / Copernicus. Dashed line *A*-*B* shows the location of the geological cross section in Figure 2.

2.2 Background Geology

Leeds does not overlie a recognised principal aquifer (Allen et al., 1997; Jones et al., 2000) but so-called 'secondary' aquifers which nonetheless possess potential for geothermal development (Boon et al., 2019), and may be sufficiently porous (via matrix or fracture porosity) to yield groundwater at the local scale (Jackson et al., 2024). Historic boreholes around Leeds, and adjacent to the UoL campus, have variously exploited these shallow

aquifers. For the UoL Geothermal Campus, the main target aquifer is a sandstone-rich interval belonging to the Carboniferous Elland Flags formation, a lithostratigraphic division of the Pennine Lower Coal Measures (Waters et al., 1996). The second, deeper, aquifer target was the Rough Rock and Rough Rock Flags, of the uppermost Millstone Grit (Hampson et al., 1996; Waters et al., 1996). Figure 2 summarises a geological cross-section under the UoL campus, informed by surface mapping and 2007 borehole (marked "SEE"). The cross-section enabled a prognostic log for the PW02a site to be constructed and, on coring PW02a, depths to the Elland Flags and Rough Rock units were confirmed as 38-92 m bgl (metres below ground level) and 198-226 m bgl respectively.

Outcrop samples of the Elland Flags sandstones suggest moderate matrix porosities but low permeabilities, corroborated during routine core analysis of plugs from the pilot wells. Flow potential is thus reliant on fracture-derived porosity and permeability. During initial pump testing in UoL's open loop boreholes, the main Elland Flags aquifer was able to sustain flow rates of up to 27.5 L s^{-1} for sustained periods. Two HOBOware loggers placed in PW02a recorded ambient temperatures of ~12.2 °C at 50 m bgl and ~12.9 °C at 100 m bgl (i.e., the top and base of the Elland Flags formation), and are used to calibrate an initial test of DTS (Figure 3) with a multi-mode fibre optic cable suspended in the borehole.

The deeper Rough Rock is a coarser sandstone, with metre-scale cross-beds but an essentially homogeneous aquifer character. It filled and buried an incised landscape during deposition therefore its thickness varies from 14 m in PW01a to 28 m PW02a. The coarser grain-sizes in the Rough Rock compared to the Elland Flags lead to a higher permeability in the rock matrix and a decreased dependence on fractures for aquifer function.

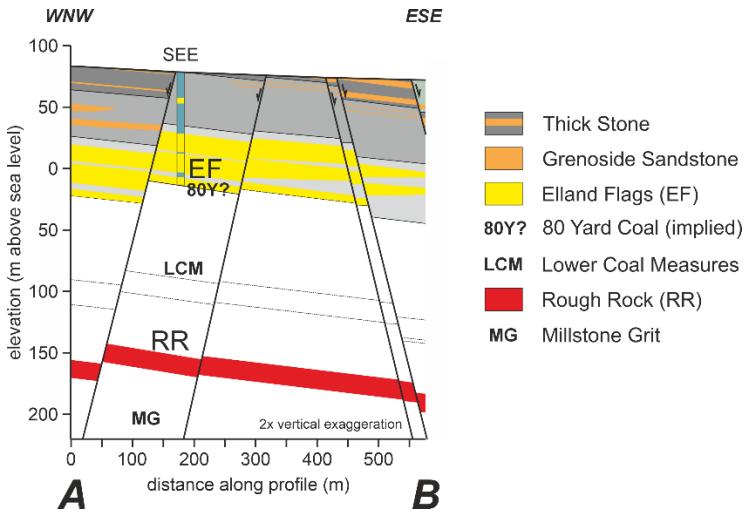

Figure 2: Geological cross-section *A-B* beneath the University of Leeds campus, showing the elevation of key units in the Coal Measures, including Elland Flags (EF) and Rough Rock (RR). Borehole 'SEE' was drilled and tested between November 2007 and January 2008, during development of the UoL School of Earth, Environment and Sustainability: this borehole is ~90 m north of PW02a, thus the mapped depths to EF and RR were usefully prognostic for PW02a.

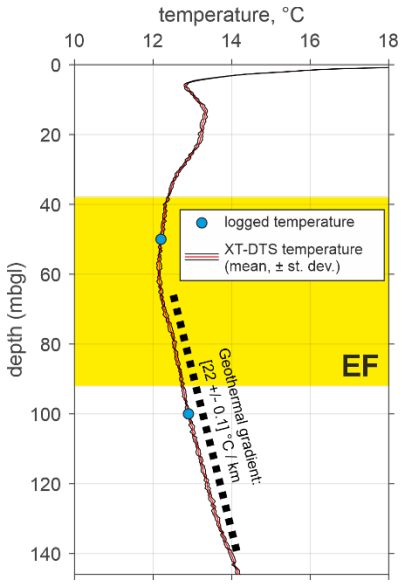

Figure 3: Temperature profile for PW02a, recorded with a Silixa XT-DTS interrogator in a suspended multi-mode fibre optic cable, and calibrated with temperature logger data. Red curve is the mean of three repeat temperature measurements, each spanning 5 minutes, with black showing the standard deviation as an error bound (typically ±0.3 °C). Spatial sampling interval is 0.25 m. Yellow shading shows the extent of the Elland Flags (EF) aquifer.

2.3 Wireline log data

In Section 3.1, we simulate DAS data based on PW02a wireline logs, but these required preconditioning to improve their reliability. Specifically, there was first a need to blend data from two closely-located boreholes, and secondly to correct a noisy sonic log.

PW02a was initially drilled as PW02, but abandoned at ~160 m depth due to a sheared well casing. PW02a was then drilled ~3 m away from the PW02 site. On the seismic scale of one Fresnel zone (Spetzler and Sneider, 2004), we consider these boreholes to sample the same

189 geology. Details of boreholes PW02 and PW02a, and the span of density and sonic logging
190 therein, are summarised in Table 1, with logs shown in Figure 4.

191 **Table 1.** Borehole details and extent of sonic and density logging in boreholes PW02 and
192 PW02a

	PW02	PW02a	Comment
Coordinate of borehole top	53.80493°N, 1.55647°W	53.8049°N, 1.55646°W	Located within 3 m of each other.
Elevation of borehole top (m above sea level; OSGB36(15) datum)	67.397	67.206	
Total depth (m)	~160	250	
Sonic log span (m)	40-115	113-249	Sonic log noisy throughout PW02.
Density log span (m)	10-108	106-249	Gap in coverage between 43-46 m in PW02.

193

194 A combined log was created, blending observations made in PW02 and PW02a and using the
195 2-3 overlap between logged ranges as calibration. Within this overlap, inconsistencies in
196 density (0.19 ± 0.05 g cm^{-3}) and slowness (23.3 ± 31.0 ms m^{-1}) were observed, hence the
197 density and sonic logs in PW02 were bulk-shifted by these amounts (grey, Figure 4b). A gap
198 in the density log, between ~43-46 m bgl, corresponds to a zone of significant fracturing. Data
199 through this gap were linearly interpolated to obtain a continuous density log at the contractor-
200 supplied depth step of 0.01 m (Figure 4a).

201 The shifted sonic log in PW02 remained noisy and produced spurious velocity/reflectivity
202 trends in initial VSP simulations. The cross-plot of PW02a sonic and density logs (magenta,
203 Figure 4c) suggests a compatible relationship with the Gardner et al. (1974) power law and a
204 2nd-order polynomial relationship (Castagna et al., 1993) for sandstone/shale geology, whereas
205 those from PW02 (grey) are largely distributed outside of these models. PW02 sonic velocities
206 were therefore replaced with values based on a Gardner-like relationship (Gardner et al., 1974)
207 between the PW02a sonic and density logs. The least-squares predicted relationship (green,
208 Figure 4c) between these is $v_{sonic} = (0.348 \stackrel{\times}{\div} 1.048)\, \rho^{2.533 \pm 0.055}$ (sonic velocity, $v_{sonic,}$ in km s^{-1}
209 and density, ρ, in g cm^{-3}). Clusters within the bivariate histogram of PW02 logs (inset, Figure
210 4c) suggest that subsets of data may be better represented with different trends, but these define
211 spurious density:velocity relationships for the known geology. As such, the PW02 sonic log

assumes the relationship defined above from the global PW02a data distribution, critically lying between defined trends for shale and sandstone geologies in the observed data range.

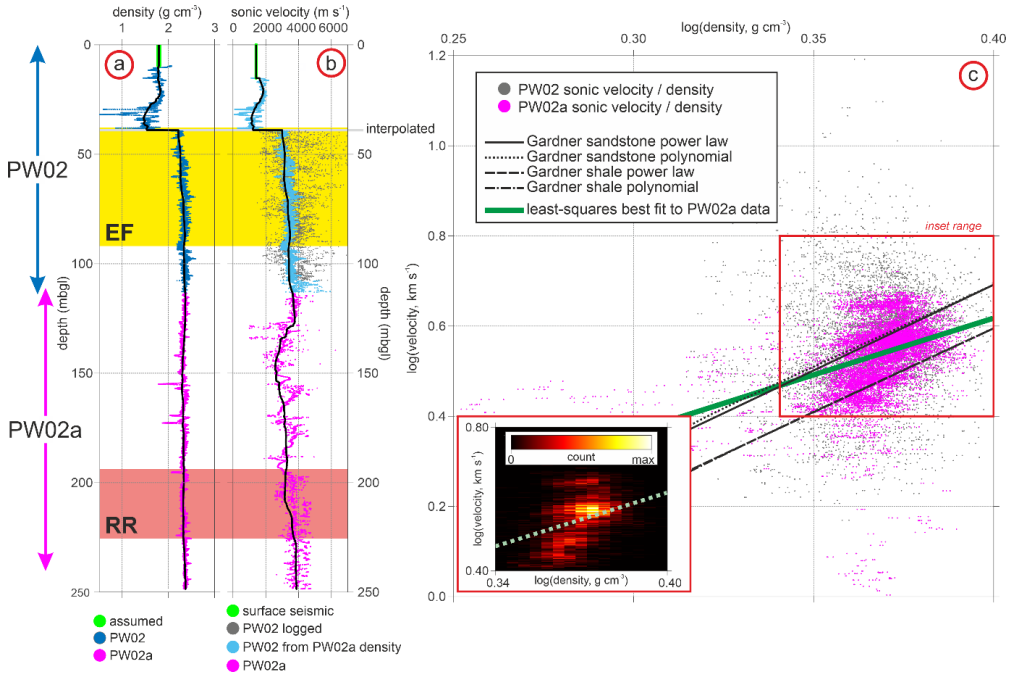

Figure 4. Wireline log data. (a) Density log, showing values measured in PW02a (magenta), and measured and shifted by 0.19 g cm^{-3} in PW02 (blue); a value of 1.8 g cm^{-3} (green) is assumed for depths < 9.6 m bgl. Black curve is the smoothed log. (b) Sonic log, showing values measured in PW02a (magenta), and measured and shifted by 23.3 μs m^{-1} in PW02 (grey); 1418 m s^{-1} (green, from seismic refraction surveying) is assumed for depths < 15 m bgl. Black curve is the smoothed log. (c) Crossplot of PW02 (grey) and PW02a (magenta) logs, and model curves for sandstone/shales. The least-squares fit to PW02a points (green) is used to define the cyan points for PW02 in (b). *Inset:* bivariate histogram through the main distribution of PW02 datapoints (density and velocity ranges discretised into bins of dimension 0.004 and 0.002 units, respectively); dashed line is the least-squares fit shown in (c). Yellow shading again shows the extent of the EF aquifer; red shading shows the Rough Rock (RR).

For simulating VSP data, the completed logs (black, Figures 4a,b) were smoothed with a running average (Liner, 2004) using a depth range approximating the wavelength-scale of recorded P-waves (10 m from 0-40 m bgl, 20 m thereafter, assuming ~100 Hz wavelet frequency). The shallowest properties (green, 0-15 m bgl) were infilled using i) a velocity of 1418 m s^{-1}, the deepest velocity sampled in a short P-wave surface refraction survey crossing

PW02 and PW02a, and ii) a representative density (1.8 g cm^{-3}) for near-surface engineering materials. Despite these corrections, data shallower than ~35 m bgl remain noisy and imply densities and velocities that are unrealistically low, potentially attributable to partial saturation and air-fill in the borehole above the water table. However, no further correction is made in this range. Furthermore, although sonic velocities were measured at 23 kHz, we omit any velocity scaling for dispersion; however, the observed difference between sonic and seismic velocity data is used to evaluate the seismic quality factor (Section 4.1).

3. DAS data: simulation and acquisition

3.1 Data simulation

DAS VSP data were simulated to predict the strength of reflectivity, without the complicating impacts of (e.g.) poor cable coupling or ambient urban noise. Our simulation used the smoothed velocity and density models from Figure 4, and fixed the ratio of compressional-to-shear wave velocities at 2 (consistent with velocity ratios later observed in Section 3.2). The free-surface is included in the model, and multiple reflections are indeed evident in simulated data. This 1-D simulation initially derived the ground displacement as a function of time at each point in depth, from 0-250 m bgl, corresponding to the centre of each gauge of the DAS recording. In the absence of field observations, we ignore attenuation and impose P- and S-wave quality factors (Q_P and Q_S) of 1000 and 500, respectively. To maintain computational tractability, we downsample the 0.01 m-spaced log to 1 m spacing, but preserve all depth points where there is a change in P-wave velocity or density larger than 10% between layers in the model. No significant differences between original and downsampled models could be observed, hence downsampling serves the prognostic purpose of our simulation.

We use the matrix propagator method of Wang (1999) to compute synthetic seismograms for a vertical-component receiver directly above the well at the surface and an explosion source at each depth; from the principle of reciprocity this is equivalent to the VSP source being placed at the surface and the recordings at depth. We then differentiate the ground displacement with respect to time to obtain ground velocity, integrate with respect to distance (equivalently, depth) along the cable to give the strain rate, and finally convolve in distance with a box-car function of width equal to the gauge length (e.g., Kennett, 2024) to reproduce the averaging effect of the interrogator. The gauge length was set to 5 m,

consistent with that used in the data acquisition (see Section 3.2). Because the source and receiver are aligned vertically and the fibre is also vertical, there is no explicit need to account for the fibre's directional sensitivity to strain.

Simulated data are shown in Figure 5, highlighting key arrivals that include the downgoing direct wave (solid red), upgoing primary reflections (blue) and multiple arrivals (purple). On encountering the strong velocity increase at ~40 m depth, consistent with the Elland Flags, the slope of direct P-wave arrivals shows a strong deviation; correspondingly, the contact with the Elland Flags produces strong reflections and is a prominent multiple-generating interface.

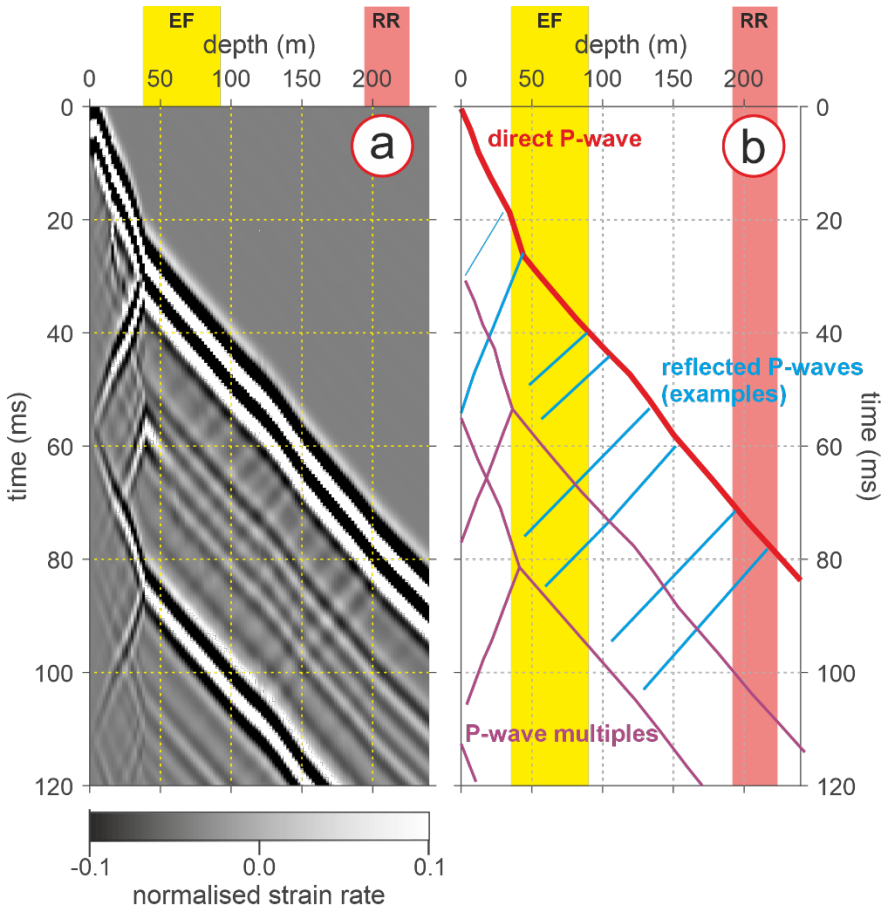

Figure 5. (a) Simulated DAS data and (b) identification of representative arrivals therein. As a 1-D synthetic, S-waves are omitted from this simulation.

3.2 Active-source DAS survey

279 The motivation for DAS surveying was to verify that the grouted cable was well-coupled,
280 and assess the extent to which poorer coupling in the ungrouted cable sections was
281 associated with reduced data quality. In PW02a, the ungrouted intervals span 37-80 m bgl
282 and 198-250 m bgl, within the Elland Flags and Rough Rock aquifers. Hudson et al. (2025)
283 show that usable data may still be obtained even where coupling is notionally poor, but
284 validating cable performance is particularly important given that the slotted intervals
285 correspond to the target geothermal reservoirs: Gurevich et al. (2023) highlight how
286 relatively small changes to casing design can impact recorded DAS amplitudes. However,
287 in anticipation of there being no such problems, the DAS acquisition was parameterised to
288 yield a high-resolution vertical velocity model.

289 The tight-buffered cable in PW02a was monitored using a Febus Optics A1 interrogator,
290 with the connection to the installed cable section made through a 1000 m-long launch cable.
291 The gauge length in the A1 interrogator can be customised and, based on the anticipated
292 smallest seismic wavelengths (a minimum of 20 m, assuming 100 Hz source frequency
293 travelling at 2000 m s^{-1}), is set to 5 m. Output data have a trace interval of 1.6 m and an
294 output time sampling interval of 0.5 ms, with no downsampling from the original pulse
295 interval.

296

297 Vertical seismic profiles (VSPs) were generated using a 6.4 kg sledgehammer source. A
298 polymer impact plate was positioned close to the top of the borehole (within 0.5 m),
299 effectively providing zero-offset data. To facilitate stacking, 38 individual impacts were
300 recorded. For our specific interrogator, recording cannot be directly activated by an impact
301 trigger (although this functionality exists in later models), therefore impact times were
302 measured directly within the passively-recorded DAS dataset. Tap-testing confirmed the
303 position (to within ± ½ gauge length) of the zero-depth trace, and individual shots were
304 identified and extracted using RMS-amplitude thresholding within this trace. The timing
305 of source impacts was initially investigated through first-break time picking, but this
306 proved difficult given noise in the records. Instead, wavelet maxima (typically, in the
307 second half-cycle of the wavelet) were picked, with first-break times then simulated by
308 shifting these picks by -10 ms, corresponding to ¾ of the 13 ms period of a 75 Hz wavelet
309 (see spectra in Figure 6). These simulated first-break times are therefore considered to be
310 the source impact time for each shot, and seismic records of 200 ms duration are extracted
311 from these times, from the continuous DAS record.

Although the hammer source can be vulnerable to a lack of repeatability, we observed a mean correlation coefficient of 0.91 between wavelets in individual shots and an arbitrary reference shot (here, shot 15 in the sequence). Correlation coefficients for a receiver at 14.4 m depth are shown in Figure 6a, considering each shot's direct arrival and comparing it (arbitrarily) to that in shot 15. Wavelets from representative shots (blue emphasis in Figure 6a) are shown in Figure 6b alongside the reference wavelet, with spectra shown in Figure 6c. A subset of 25 shots was selected for stacking, comprising those for which the correlation coefficient with the reference shot exceeds 0.9 and only those which increased the cumulative signal-to-noise ratio (SNR) in the stack. Following stacking, SNR was increased from ~2 dB (Figure 7a) to ~18 dB (Figure 7b).

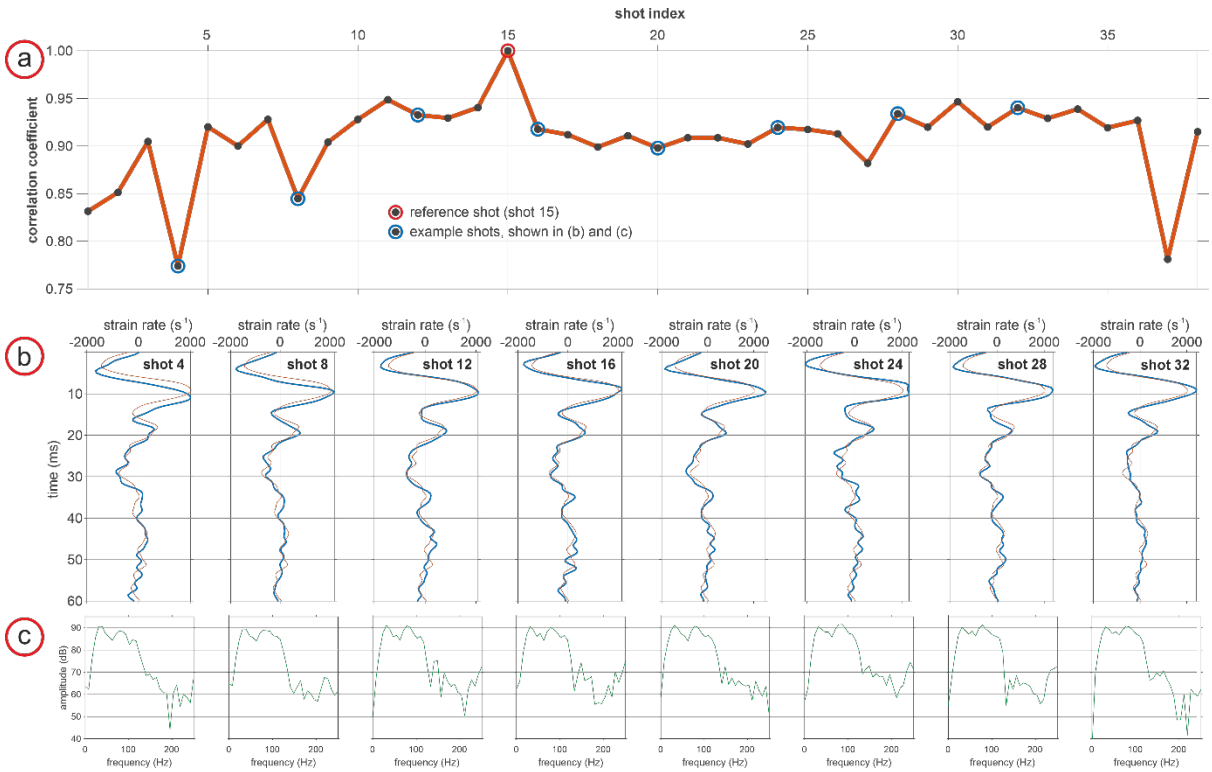

Figure 6: Correlation metrics for a sequence of 38 hammer strikes. (a) Correlation coefficients of traces recorded at 14.4 m depth, with respect to a reference trace from shot 15. (b) Traces from selected shots, shown in blue, and the reference trace from shot 15. (c) Amplitude spectra

of panels in (b). Throughout, an Ormsby bandpass filter (corner frequencies 5-10-200-400 Hz) is applied.

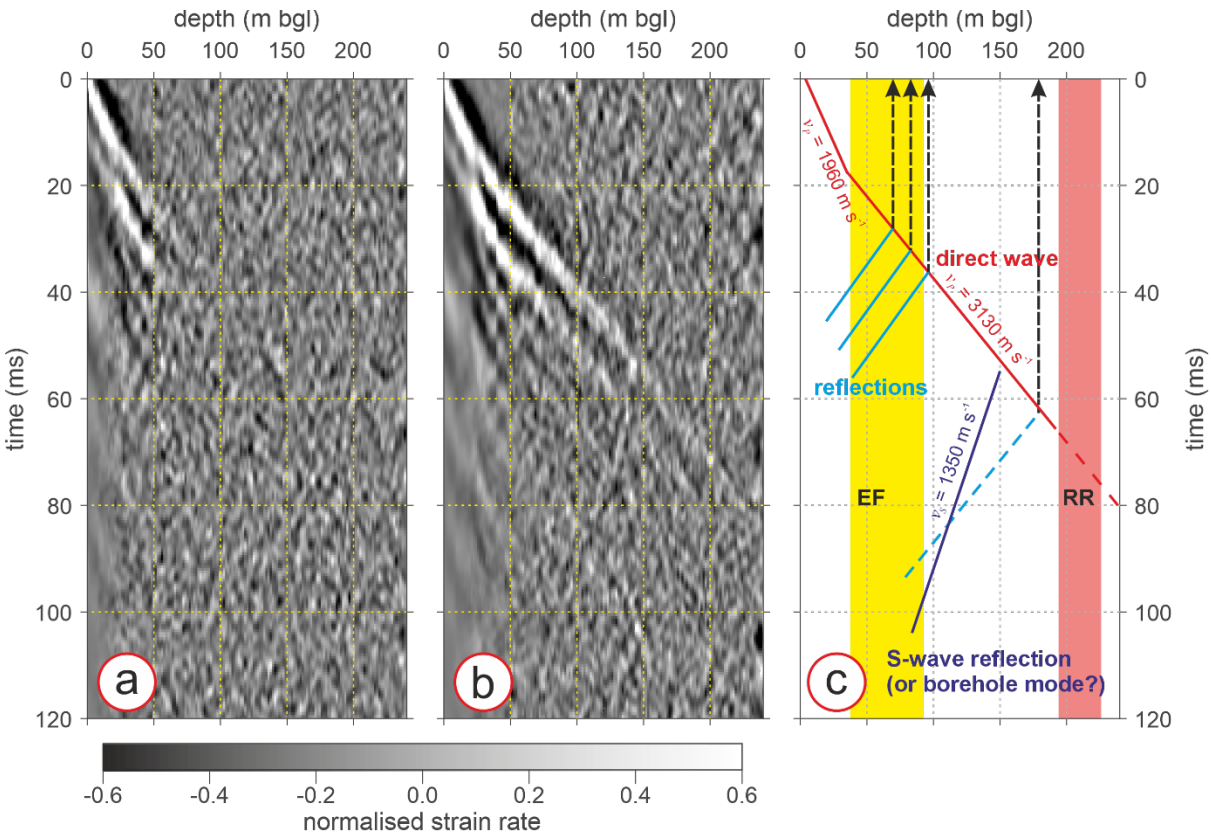

Figure 7: DAS data from PW02a. (a) Shot 15 in the sequence of 38 shots. (b) An optimised stack of 25 shots, based on metrics defined in main text and Figure 6. (c) Initial appraisal of data, identifying representative direct wave velocities, suggested reflectivity and a likely shear-wave reflection. Data displays have an Ormsby bandpass filter (corner frequencies 5-10-200-400 Hz) applied.

The initial appraisal of direct wave amplitudes shows no local reductions in SNR that can be associated with ungrouted zones (37-80 m bgl and 198-250 m bgl). The cable also appears to be intact through its whole length, with arrivals still perceptible (albeit with low SNR) in the deepest traces that sample the Rough Rock aquifer. Consistent with the synthetic data, the slope of direct wave arrivals undergoes a distinct change at 40 m depth, likely across the water table and into the Elland Flags aquifer; the coarse v_P model is also consistent with the wireline velocity log: ~2000 m s^{-1} in the upper 40 m, increasing to

~3100 m s^{-1} thereafter (Figure 7c). The direct wave arrival times display a slight inflexion at ~150 m bgl, indicating a local velocity anomaly, which is also observed in the synthetic data.

Although the sequence of primary reflectivity is altogether weaker and sparser than implied in the simulation, a package of P-wave reflections is perceptible between 50-95 m bgl, likely from within the Elland Flags; more isolated reflectivity could be present at greater depth (e.g., a weak event around 180 m bgl). Frequency-wavenumber filtering was attempted to boost the clarity of reflections but this was of limited value, likely due to poor signal-to-noise ratio at depth. A further reflection originates from ~150 m bgl, which expresses a velocity (~1350 m s^{-1}) that is slower than any direct P-wave. Although the orientation of our cable is unfavourable for recording S-waves, we assume that this arrival is some S-wave phase from a dipping horizon or fracture, or alternatively some borehole mode.

The shallowest ~18 m of data appear dominated by near-surface reverberations, which destructively interfere and remove any coherent arrivals in this interval. Unlike the synthetic, discrete multiple arrivals are not apparent elsewhere, likely because of the apparent weakness of primary reflectivity in the first instance. Furthermore, attenuation was effectively neglected in the synthetic, thus Q_P is greatly over-estimated. An initial depth-averaged Q_P estimate is obtained by considering the amplitude decrement within the depth interval z_1 to z_2. Neglecting reflectivity effects, the amplitude A_2 observed at z_2 can be expressed as

$$A_2 = A_1 \, (z_1/z_2) \, e^{-\alpha(z_2 - z_1)} \qquad (1)$$

where A_1 is the amplitude observed at z_1, (z_1/z_2) is the contribution to amplitude loss from geometrical spreading and α is an attenuation coefficient, related to Q_P as $\alpha = \pi / Q_P \lambda$. Direct wave amplitudes A_1 and A_2 were measured across three traces (i.e., one gauge length) in traces centred on z_1 = 44.8 m and z_2 = 140.8 m; A_1 and A_2 are 8167 ± 2200 and 1769 ± 400. Rearranging equation (1), α is estimated as 4.0 ± 0.2 km^{-1}. With f = 75 Hz and $v_P \approx$ 3100 m s^{-1}, Q_P is 19 ± 2.

4. Interpretation

4.1 Vertical velocity models

A depth-varying v_P model is obtained using the cross-correlation lag between direct wave arrivals in pairs of traces separated by a fixed gap (e.g., Booth et al., 2020). To reduce the discretisation in cross-correlation time steps, the temporal sampling interval in the data was upsampled to 0.1 ms; a bandpass filter (10-20-75-150 Hz corner frequencies) was applied, together with muting to isolate the direct wave (Figure 8a). The DAS-derived velocity model (blue points, Figure 8b) is obtained using a correlation gap of 40 m depth: longer gaps produced models that were deemed to be over-smooth, whereas smaller gaps were prone to noise and featured large velocity jumps across small intervals. Nonetheless, correlation lags required manual adjustment beyond 75 m depth, where the peak cross-correlation produced spurious velocities (e.g., where the correlation diverged from the first half-cycle of the direct wave, instead matching later half-cycles and/or ambient noise). With the observed velocities and dominant wavelet frequency of 75 Hz, 40 m is also representative of the dominant wavelength in the data. Beyond ~160 m bgl (grey box in Figure 8), SNR is too poor to obtain reliable cross-correlations.

Also shown in Figure 8b is the velocity model from the wireline sonic log. The wireline points show the mean inverse slowness (and its standard deviation as an error bar) of log values within a 5 m depth range, consistent with the DAS gauge length, and are plotted every 1.6 m, consistent with the DAS trace interval. The precision of the DAS velocity model is estimated as ± 50 m s^{-1}, evaluated by simulating cross-correlations that are contaminated with amplitude-scaled noise traces from the DAS record. Direct waves are represented by 75 Hz Ricker pulses, which are delayed from a reference arrival by times ranging from 8 ms to 20 ms (equivalent to a v_P range from 2000 m s^{-1} to 5000 m s^{-1}, across a 40 m correlation gap). 1000 manifestations of noise traces are added to these models, with SNR ranging from 10 to 30 dB. Figure 9 shows the standard deviation of inverse slownesses for these delay times and SNR pairs, across these 1000 noise manifestations. As stated in Section 3.2, the typical SNR we observe is 18 dB, and the mean v_P in Figure 7b is ~3100 m s^{-1}, which corresponds to a time lag of ~13 ms across the correlation gap.

For these model parameters, Figure 9 implies that the standard deviation of inverse slownesses is ±50 m s^{-1}.

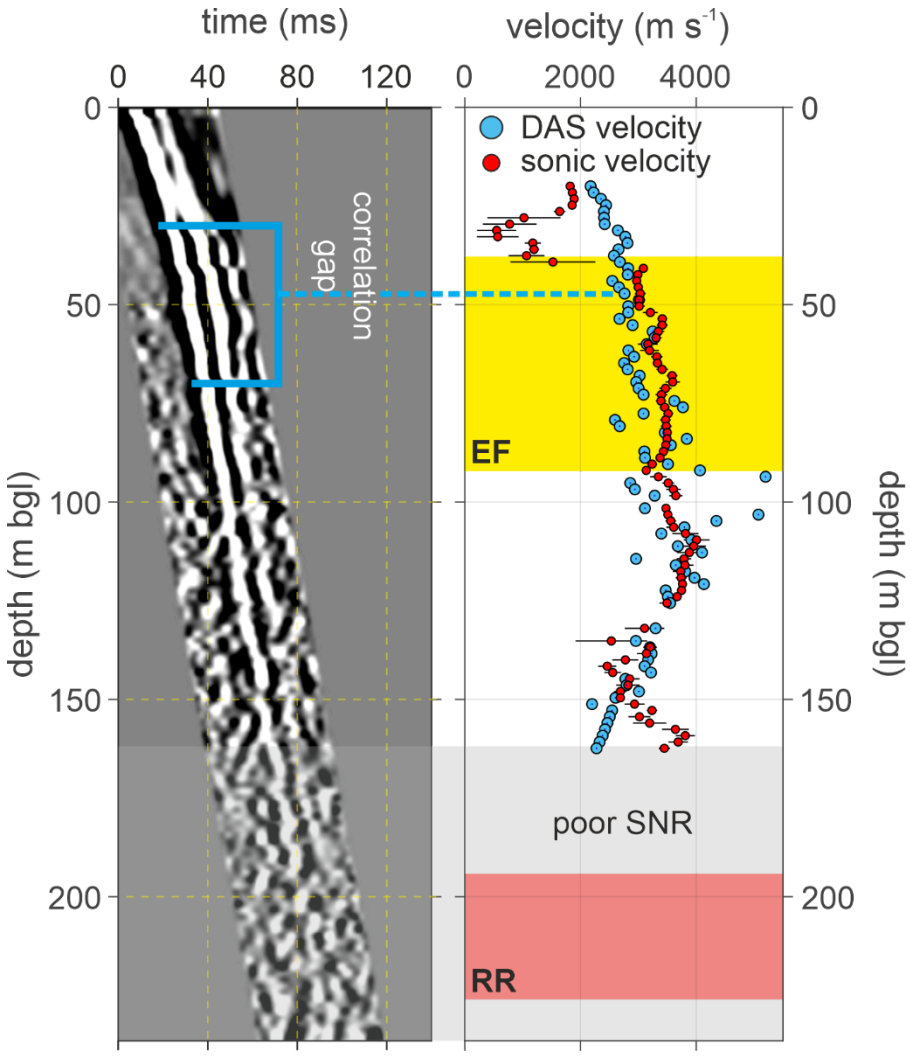

Figure 8: Velocity analysis of DAS VSP direct wave. a) Direct wave, isolated and bandpass filtered. The display is rotated with respect to earlier figures, for better comparison to velocity models. The blue bar shows the length of the cross-correlation gap, an indicator of the resolution of the DAS-derived velocity model. b) Velocity models derived from (blue) cross-correlation of direct waves in DAS and (red) the wireline sonic log in Figure 4b. DAS points are plotted at the centre of the correlation gap.

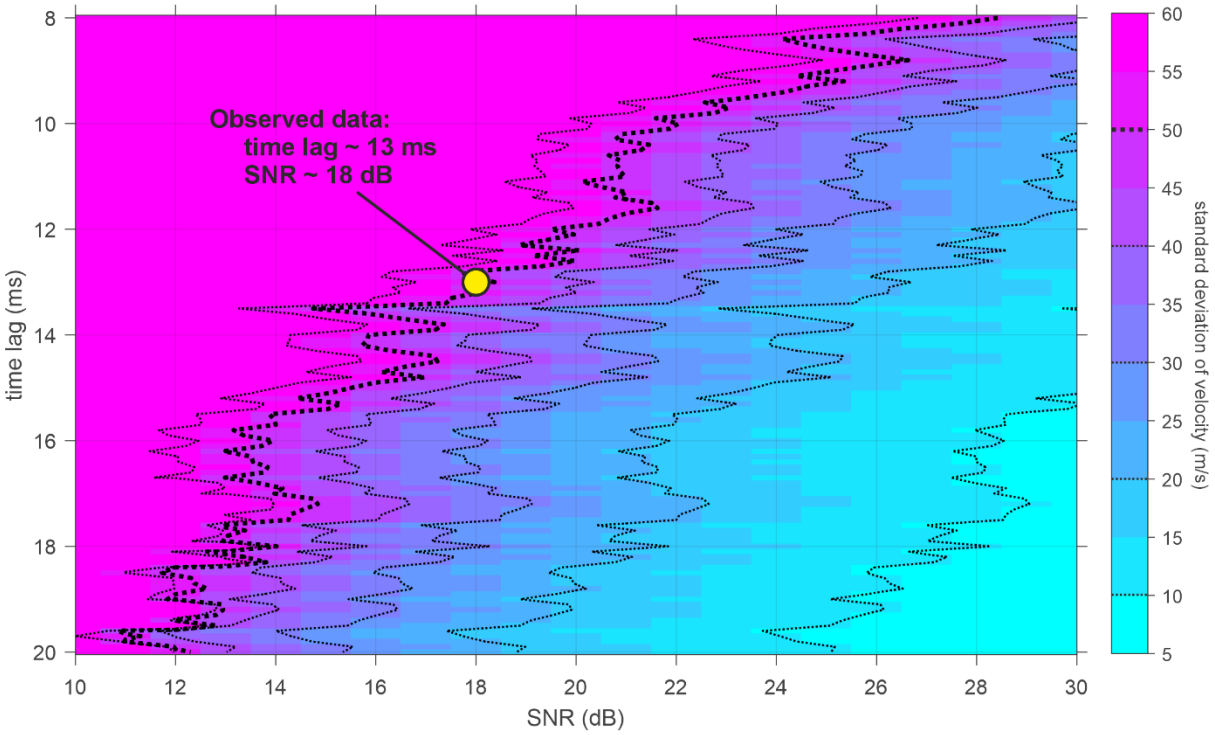

Figure 9: Estimation of precision for DAS-derived velocity model. For SNR = 18 dB and a time lag of 13 ms across the 40 m correlation gap (v_P = 3100 m s^{-1}), 1000 manifestations of random noise traces imply a standard deviation of inverse slowness of ±50 m s^{-1}. Contours are at 10 m s^{-1} intervals; the 50 m s^{-1} contour is shown in bold.

The DAS-derived velocity model shows similar behaviour to the sonic log (red, Figure 8b), with v_P steadily increasing from ~2500 m s^{-1} at 40 m depth, through the Elland Flags aquifer, and reaching ~4000 m s^{-1} at 120 m bgl. Velocity reduces between 120-160 m bgl, although the sonic and DAS models diverge in the lower 20 m of the model. Consistent with the increase in reflectivity, the DAS-derived velocity model becomes chaotic in the lower section of the Elland Flags, with significant deviations in the interval 90-110 m bgl. This spans the interval of intense fracturing which led to the abandonment of borehole PW02. In the uppermost 40 m of the log, in the unsaturated zone above the water table, the DAS-derived velocity model appears to give more reliable data than the sonic log.

Nonetheless, DAS velocities are systematically lower than the sonic velocities (especially through the Elland Flags aquifer) due to dispersion, and the difference can be used to evaluate Q_P. Liner (2004) provides an expression for Q_P that is not limited to low-loss media (i.e., permitting Q_P < ~100) which states

$$\frac{v_{f_1}}{v_{f_2}} = \left(\frac{f_1}{f_2}\right)^{\gamma}, \quad (2)$$

where

$$\gamma = \frac{1}{\pi} tan^{-1}\left(\frac{1}{Q_P}\right) \quad (3)$$

and v is the propagation velocity observed at frequencies f_1 and f_2 (set here at 23 kHz and 75 Hz, respectively, for sonic and DAS observations). The right-hand-side of equation (2) is the gradient in a linear regression between v_{f_1} and v_{f_2}, with the intercept set to 0, i.e.

$$v_{f_1} = \left(\frac{f_1}{f_2}\right)^{\gamma} v_{f_2} \quad (4)$$

The best-fit regression is defined as the geometric bisector between regressions obtained when v_{f_1} and v_{f_2} are interchanged between x and y axes, which honours the associated uncertainty in both observations. Figure 10 cross-plots the DAS- and sonic-derived velocity models, and shows the best-fit regression lines for all points from depth > 40 m bgl (red dashed line) and for points within the Elland Flags aquifer (solid red line). Points which plot beneath the $Q_P = \infty$ are considered non-physical. Given the unreliability of the shallow sonic log, this is the case of all points < 40 m bgl hence they are excluded. Some deeper points show this behaviour too, but we include them in our calculation for statistical rigour.

The overall regression line defines $Q_P = 36 \pm 5$; this reduces to $Q_P = 30 \pm 2$ when considered only through the Elland Flags, potentially due to the greater degree of fracturing. We recognise that the comparability of sonic and DAS data may be limited, given that the different operational frequencies and measurement lengths (e.g., the ~2 m length of the sonic logging tool vs. the 40 m correlation gap for DAS) implies that different spatial scales of geology are sampled around the borehole. However, this is represented in the scatter in the data and thus accommodated in the uncertainty bounds on results. Furthermore, these observations are comparable with Q_P estimates made in Section 3.2 m, based entirely on DAS data.

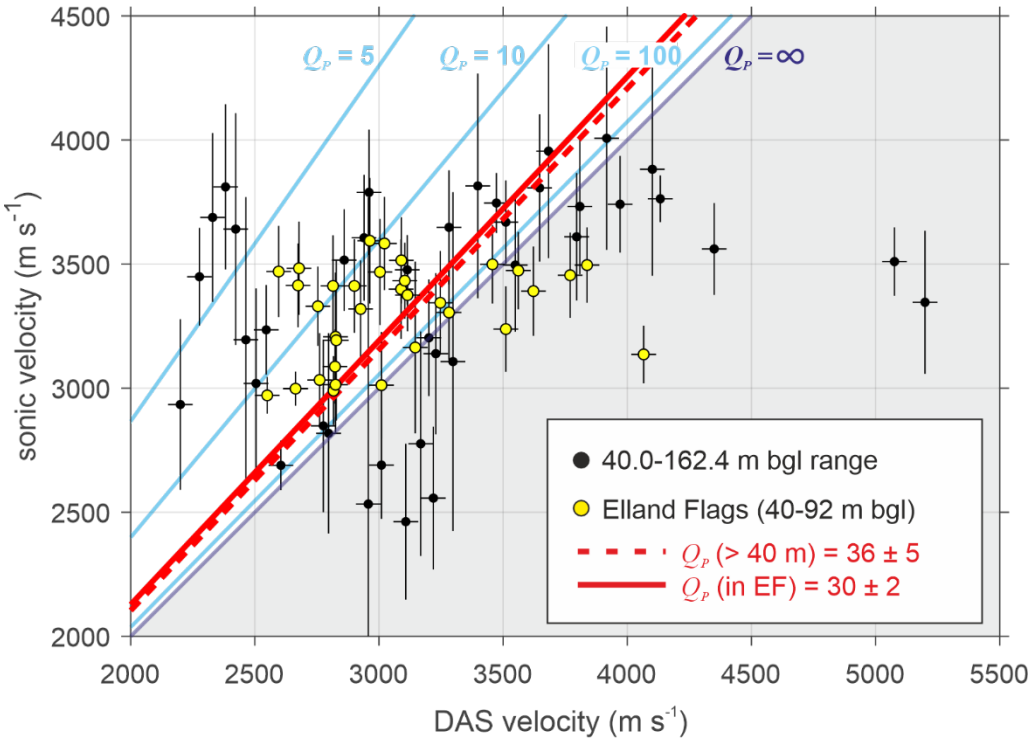

468

469 **Figure 10:** Cross-plot of DAS- and sonic-derived velocity models, for depth > 40 m bgl.
470 The slope of the linear regression (red lines) provides the right-hand-side of Equation (2),
471 and thereby the Q_P when f_1 is 23 kHz and f_2 is 75 Hz. Blue lines indicate reference slopes
472 for Q_P of 5, 10 and 100. Datapoints which plot beneath $Q_P = \infty$ (grey shading) are
473 considered non-physical.

474

475 **4.2 Temperature sensitivity of seismic velocity**

476 Having shown that our DAS installation is compatible with obtaining reliable seismic
477 properties, we now consider the likelihood that a given temperature change results in a
478 detectable velocity change. Then elastic properties of water vary with temperature (Poletto et
479 al., 2018; Fokker et al., 2024) and therefore modify v_P and Q_P from a reference value. For the
480 purposes of this feasibility study, we consider only a static model of elastic properties and only
481 simulate the v_P response; we omit the dynamic behaviour (e.g., squirt flow; Poletto et al., 2018)
482 that would be needed to predict the behaviour of Q_P.

483 We apply the Hashin-Shtrikman (HS) model (Mavko et al., 2020) to predict the seismic
484 response of the Elland Flags aquifer to different heating and cooling scenarios. The HS model
485 predicts the widest possible range of elastic moduli given the bulk (κ) and shear (μ) modulus
486 of constituents and their volume fraction, while making no assumptions about the matrix

architecture of a rock. The upper bound of the precited range gives the stiffest possible assemblage: the stiffest bulk modulus κ_{HS}^{+}, is

$$\kappa_1 + \frac{\phi_2}{(\kappa_2-\kappa_1)^{-1}+\phi_1\left(\kappa_1+\frac{4}{3}\mu_1\right)^{-1}} \qquad (5)$$

and the stiffest shear modulus, μ_{HS}^{+}, is

$$\mu_1 + \frac{\phi_2}{(\mu_2-\mu_1)^{-1}+2\phi_1(\kappa_1+2\mu_1)/\left[5\mu_1\left(\kappa_1+\frac{4}{3}\mu_1\right)\right]^{-1}} \qquad (6)$$

where ϕ_1 and ϕ_2 are the fractions associated with constituent moduli $\kappa_{1,2}$ and $\mu_{1,2}$. The lower bound describes the softest possible assemblage, and is expressed when the constituents associated with indices 1 and 2 are swapped. When combined with a volumetric average density, the possible range of v_P is

$$v_P^{\pm} = \sqrt{\left(\kappa_{HS}^{\pm} + \frac{4}{3}\mu_{HS}^{\pm}\right)/\rho} \quad . \qquad (7)$$

When one of the constituents is a fluid, as in the case we model here, the upper bound is expressed as a *modified* upper bound to acknowledge a critical porosity of ~40%. At this point, the upper bound converges on the lower bound and, without this, the stiffness of highly porous materials is over-estimated. However, the difference between the modified and original upper HS bound is small at our estimated porosity of 15%.

The mineral component of the Elland Flags matrix is fixed and assumed to be quartz, with ρ = 2530 kg m^{-3} and κ = 30.8 GPa. These quantities are derived from the Elland Flags interval of the density and sonic logs in Figure 4, assuming μ = 11.6 GPa, which fixes compressional-to-shear velocity ratio at 2 (guided by the ratio, = 2.46, implied in Figure 7c). To simulate less cohesive aquifer architectures, we also simulate a velocity ratio of 5 (requiring μ = 1.3 GPa). For the water component, the model of Ewing et al. (1948) is used to describe the temperature dependency in water of v_P and κ; water density is fixed at 1000 kg m^{-3}, and its shear modulus is 0 GPa. The 15% total porosity of the Elland Flags is represented with mineral (ϕ_1) and fluid (ϕ_2) fractions set to 0.85 and 0.15 respectively. Our models represent the largest plausible change in v_P since we assume that pore water at ambient temperature is entirely replaced by water at some warmer or cooler temperature; given the low permeability of the Elland Flags, this is unlikely in a real geothermal development. Temperature loggers and DTS in PW02a record ambient temperatures of ~12 °C in the Elland Flags (Figure 3): we model cooling to a

minimum of 5 °C and heating to a maximum of 32 °C (exceeding the likely range that would be experienced in the real operation of the campus system). Within this range, we anticipate no change in the elastic properties of the quartz component of the Elland Flags (e.g., Woodman et al., 2021) and are thus justified in varying only the properties of the pore water.

Figure 11 shows the v_P change in the Elland Flags with changing water temperature, for the lower (solid red) and modified upper (dashed red) HS bounds. Our limit of sensitivity is defined as ± 50 m s^{-1} (i.e., $\delta v/v$ ~1.6%), the precision threshold in our correlation-based velocity analysis. The green-shaded areas of Figure 11 show where the implied velocity change exceeds the ± 50 m s^{-1} sensitivity threshold. If the architecture of the aquifer conforms with the lower HS bound (i.e., a soft assemblage of mineral and fluid components), we suggest that our approach could only detect the expression of heating when > 26 °C, and is insensitive to cooling. If the Elland Flags architecture was instead more consistent with the upper HS bound (e.g., the stiffest possible assemblage), then plausible temperature increases may be undetectable. However, for the structurally weaker aquifer described by the blue HS bounds, the range of plausible velocities is narrower and there is more likelihood that the expression of heating could be detected.

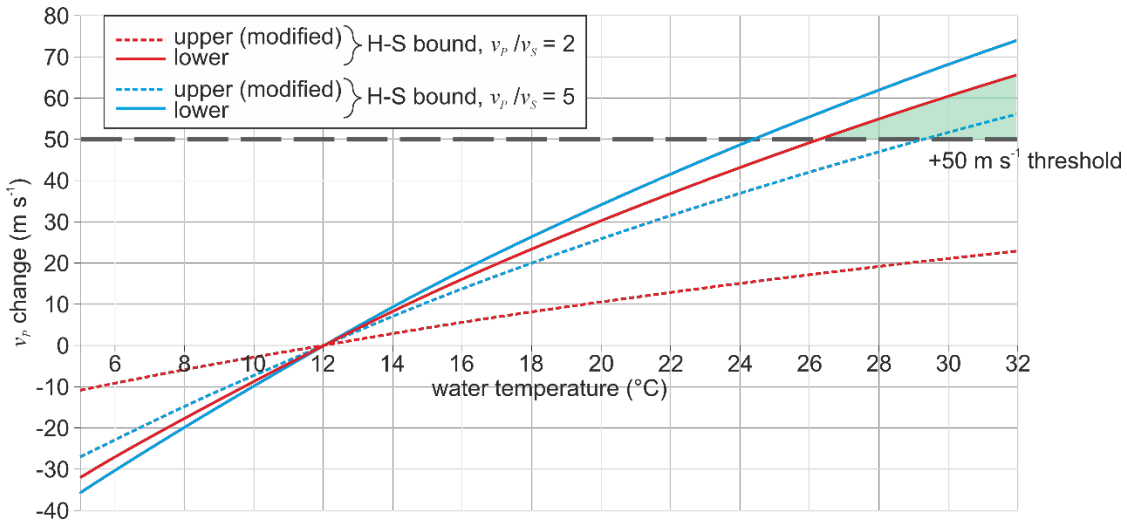

Figure 11. P-wave velocity anomaly as a function of water temperature in the Elland Flags aquifer. Red lines show the lower (solid) and modified upper (dashed) Hashin-Shtrikman bounds for v_P/v_S = 2, with the green shading highlighting where the v_P anomaly exceeds our precision threshold of 50 m s^{-1} sensitivity threshold (thus only visible for the heating scenario). For comparison, the blue lines are the Hashin-Shtrikman bounds for a less cohesive aquifer with v_P/v_S = 5.

Although dynamic behaviour is omitted from this model, an increase in v_P would change the apparent Q_P. If all velocities through the EF were increased by 50 m s^{-1} (i.e., the upper bound of velocity precision), the regression line in Figure 10 would instead define 41 ± 3, which is statistically distinct from the original Q_P (30 ± 2). This suggests that Q_P may be the more sensitive indicator of heating, although a more complex model (e.g., Poletto et al., 2018) would be required to explore this fully.

5. Discussion: Precision of DAS velocity models and their utility

In modelling the behaviour of an aquifer thermal energy storage (ATES) site, Jackson et al. (2024) suggest that groundwater temperature changes in plausible usage scenarios would most likely be ~5 °C, and would be unlikely to exceed 8 °C. In the Elland Flags, based on inferences from Figure 11, these changes would represent $\delta v/v$ of ~0.5% and ~0.7%, respectively. Our current approach therefore lacks the sensitivity to detect thermal variations of this magnitude, although could potentially be used to support UK environmental legislation that restricts temperature increases above 25 °C. There is also increasing interest in developing underground thermal storage solutions which could lead to higher routine temperatures (Bloemendal et al., 2024), subject to updated regulatory oversight and approval (Gonzalez Quiros et al., 2025)

Improved sensitivity could be provided by modifications to the acquisition approach, thereby improving SNR, or a more sophisticated approach to velocity model building. For the former, a more impactful seismic source could be considered, or a longer gauge length (although this comes at the detriment of depth resolution). To resolve a temperature change of +5 °C (i.e., a velocity change of +20 m s^{-1}), Figure 9 suggests that SNR would need to be raised above 25 dB. For improving the velocity estimate, techniques such as coda wave interferometry could be highly sensitive to localised velocity anomalies. Ouellet et al. (2025) confidently detect $\delta v/v$ anomalies of 1% in geotechnical DAS data, and Li et al. (2025) show sensitivities to $\delta v/v$ perturbations less than 0.5% associated with temperature-related stress fluctuations. Extensive passive recordings are currently not available for the UoL campus, but will be explored during forthcoming thermal tests.

Although our existing approach may lack the sensitivity for detailed thermal monitoring, our DAS-derived velocity models likely suffice for seismic stratigraphic correlation across campus. The location of boreholes was, in part, informed based on the known location of faults beneath campus (see Figure 2), since these potentially impact hydraulic connectivity However, it is highly possible that additional faults are present. Only a subset of boreholes were cored and logged, to provide depth control on the key horizons such as the target aquifers. For the remaining boreholes, the depth to (and, potentially, the properties of) the Elland Flags aquifer could be resolved using DAS. One diagnostic characteristic of the velocity model (Figure 8) could be its systematic reduction ~20 m beneath the EF. If this was consistently observed in other boreholes, it allows the maximum extent of the EF to be predicted at unlogged locations.

However, even if the sensitivity of DAS to small-scale thermal change could be verified, the current cost of interrogators likely limits the widespread uptake of DAS in geothermal monitoring. However, given that shallow geothermal systems can achieve the greatest impact in the urban environment, co-located dark-fibre networks (passively monitoring, e.g., traffic noise and, indeed, induced seismicity) could support in-borehole measurement while reducing the cost of cable installation (e.g., Ehsaninezhad et al., 2025).

6. Conclusions

Geothermal living-labs provide vital research infrastructure for advancing geophysical monitoring technologies that can track the thermal evolution of the subsurface. In this paper, using boreholes on the University of Leeds Geothermal Campus, we have explored the characteristics of an active-source DAS dataset, and derived baseline models of compressional wave velocity and quality factor. Through petrophysical modelling using the Hashin-Shtrikman framework, we predicted the likely sensitivity of our experimental approach to thermally-induced changes in elastic properties. For the Elland Flags aquifer, we suggest that groundwater heating could only be detectable if it exceeded 25 °C. While this may help monitor environmental compliance, improved approaches to both data acquisition and velocity modelling could improve the sensitivity of seismic properties to more subtle expressions of thermal change.

Data availability

The sequence of 38 DAS shots, and the velocity model and QSEIS input used to generate synthetic DAS data, are available in figshare repository "*Seismic data and forward models from the University of Leeds Geothermal Campus, borehole PW02a, October 2024*", 10.6084/m9.figshare.32366394.

Conflict of interest statement

The authors declare no conflict of interest.

Acknowledgments

We thank three anonymous reviewers and editor Ayse Kaslilar Sisman for constructive comments that improved the quality of this manuscript. The Geothermal Campus living lab facility is funding by the University of Leeds as part of its Climate Plan. The DAS equipment used in this study is from the University of Leeds Fibre-Optic Facility, with acquisition funded through loan UOL-FOF-0007 by the Leeds Geosolutions centre as part of the University of Leeds Climate Plan (Principle 3). The QSEIS code for calculating synthetic seismograms with the matrix propagator method of Wang (1999) is available at https://git.pyrocko.org/pyrocko/fomosto-qseis/. AN was funded by Geosolutions (project 'Sustainable subsurface resource management with testable geophysical and geological models') and NERC (grant 'Mantle Circulation Constrained (MC2): A multidisciplinary 4D Earth framework for understanding mantle upwellings'; NE/T012684/1). RM contributed to this work during a student dissertation project on the University of Leeds' MGeophys Geophysics programme. JK is supported by an EPSRC DTP studentship. Core description by RC is supported by University of Leeds GeoCoDA funds.

REFERENCES

Abesser, C., Busby, J.C., Pharoah, T.C., Bloodworth, A.J. and Ward, R.S.: Unlocking the potential of geothermal energy in the UK (2020). *British Geological Survey Open Report*, OR/20/049.

Allen, D.J., Brewerton, L.J., Coleby, L.M., Gibbs, B.R., Lewis, M.A., MacDonald, A.M., Wagstaff, S.J. and Williams, A.T. (1997). The physical properties of major aquifers in England

635 and Wales. British Geological Survey Technical Report WD/97/34. 312pp. Environment
636 Agency R&D Publication 8.

637 Azzola, J., Thiemann, K. and Gaucher, E. (2023). Integration of distributed acoustic sensing
638 for real-time seismic monitoring of a geothermal field. Geothermal Energy, 11, 30,
639 10.1186/s40517-023-00272-4.

640 Bloemendal, M., Bruhn, D., Bossennec, C., Huhn, F., Klein, S., Kranz, S., Meier, N., Peach-
641 Gibson, A., Olver, T., Peresty, V., Pham, H., Sass, I., Tym, A., and Varon, P (2024). The
642 PUSH-IT project: Geothermal energy storage demonstration and advances for different storage
643 technologies and geological settings. European Geosciences Union General Assembly 2024,
644 Vienna, Austria, 14–19 Apr 2024, EGU24-18418, 10.5194/egusphere-egu24-18418.

645 Boon, D.P., Farr, G.J., Abesser, C., Patton, A.M., James, D.R., Schofield, D.I., & Tucker, D.G.
646 (2019). Groundwater heat pump feasibility in shallow urban aquifers: Experience from Cardiff,
647 UK. Science of the Total Environment, 697, 133847.

648 Boon, D., Hough, E., Thompson, J., Al-Jawad, J., Gonzalez Quiros, A., Haslam, R., Raine, R.,
649 Cripps, C., Spence, M., Hetherington, D., Croft, J., Smith, H., Cresswell, S., Scott, L., Findlay,
650 J., Taylor, K., Ma, L., Hao, J. and Jackson, M. (2025). Multi-scale thermal property
651 characterisation of a UK Triassic sandstone aquifer with relevance to ATES. European
652 Geothermal Congress, Zurich, Switzerland, 6-10 October 2025.

653 Booth, A.D., Christoffersen, P., Schoonman, C., Clarke, A., Hubbard, B., Law, R., Doyle, S.H.,
654 Chudley, T.R. and Chalari A. (2023): Distributed Acoustic Sensing of seismic properties in a
655 borehole drilled on a fast-flowing Greenlandic outlet glacier. *Geophysical Research Letters*,
656 47(13), e2020GL088148.

657 Carpentier, S., Vandeweijer, V., Petitclerc, E., Paap, B. and Verdel, A. (2020). Using fibre-
658 optic DAS surveying to de-risk a shallow geothermal energy storage site in Brussels, Belgium.
659 First EAGE Workshop on Fibre Optic Sensing, March 2020, Volume 2020, 1-4. 10.3997/2214-
660 4609.202030009.

661 Chamarczuk, M., Ajo-Franklin, J., Nayak, A., Norbeck, J., Latimer, T., Titov, A. and Dadi, S.
662 (2025). Insights into seismicity associated with flexibly operating enhanced geothermal system
663 from real-time distributed acoustic sensing. Journal of Geophysical Research: Solid Earth,
664 130(7), e2025JB031634, 10.1029/2025JB031634.

Climate Change Commission (2020): Next steps for UK heat policy. *Committee on Climate Change* (https://www.theccc.org.uk/publication/next-stepsfor-uk-heat-policy/).

Castagna, J.P., Batzle, M.L., & Kan, T.K. (1993). Rock physics – the link between rock properties and AVO responses. In '*Offset-dependent reflectivity – theory & practice of AVO analysis'.* J.P.Castagna & M.Backus (eds.) Investigation on Geophysics 8, SEG, Tulsa, OK.

Claesson, J. and Eskilson, P. (1988). Conductive heat extraction to a deep borehole: thermal analysis and dimensioning rules. Energy, 13, 509-527.

Ehsaninezhad, L., Wollin, C., Rodriguez Tribaldos, V. and Krawczyk C. (2025). Combining DAS and ambient seismic noise interferometry and unsupervised machine learning for 2D imaging of an urban subsurface. Seismological Research Letters, 96(6), 3731-3745, 10.1785/0220250056.

Environment Agency (no date). Environmental Good Practice Guide for Ground Source Heating and Cooling. GEHO0311BTPA-E-E, UK Government Environment Agency, v3. Accessed 30/01/2026 at https://mail.gshp.org.uk/pdf/EA_GSHC_Good_Practice_Guide.pdf

European Commission (2016). An EU strategy on heating and cooling. *European Commission, Brussels (https://eur-lex.europa.eu/legal-content/EN/TXT/?qid=1575551754568&uri=CELEX:52016DC0051).*

Ewing, M., Worzel, J., & Pekeris, C.L. (1984). Propagation of Sound in the Ocean. Geological Society of America Memoir 27.

Fokker, E., Ruigrok, E. and Trampert, J. (2024). On the temperature sensitivity of near-surface seismic wave speeds: application to the Groningen region, the Netherlands. Geophysical Journal International, 237(2), 1129-1141. 10.1093/gji/ggae102.

Gardner, G.H.F., Gardner L.W. and Gregory, A.R. (1974). Formation velocity and density – the diagnostic basics for stratigraphic traps. *Geophysics*, 39, 770-780.

González Quirós, A., Stewart, M., Olver, T., Klein, S., Mugova, E. and Abesser, C. (2025). Challenges and opportunities for high-temperature mine thermal energy storage with focus on regulatory barriers for implementation. *In:* Valente, T., Mühlbauer, R., Ordóñez, A. and Wolkersdorfer, Ch.: International Mine Water Association Conference – Time to Come. International Mine Water Association Conference (IMWA), Braga, Portugal (Portugal). 10.5281/zenodo.17131914.

Gurevich, B., Tertyshnikov, K., Bóna, A., Sidenko, E., Shashkin, P., Yavuz, S. and Pevzner, R. (2023). The effect of the method of downhole deployment on distributed acoustic sensor 643 measurements: Field experiments and numerical simulations. Sensors, 23(17), 644, 10.3390/s23177501.

Hampson, G.J., Elliott, T. and Flint, S.S. (1996). Critical application of high resolution sequence stratigraphic concepts to the Rough Rock Group (Upper Carboniferous) of northern England. Geological Society, London, Special Publications, 104(1), 221-246.

Hudson, T., Stork, A., Muir, J. and Fichtner, A. (2025). Unlocking DAS amplitude information through coherency coupling quantification. Seismica, 4(1), 10.26443/seismica.v4i1.1488.

Iten, M., Buhler, M., Fischli, F., Bethmann, F. and El-Alfy, E. (2024). Distributed fiber-optic temperature monitoring in boreholes of seasonal geothermal energy storage. Procedia Structural Integrity, 64, 1642-1648.

Jackson, M.D., Regnier, G., and Staffell, I. (2024). Aquifer Thermal Energy Storage for low carbon heating and cooling in the United Kingdom: Current status and future prospects. Applied Energy, 376, 124096, 10.1016/j.apenergy.2024.124096.

Jones, H.K., Morris, B.L., Cheney, C.S., Brewerton, L.J., Merrin, P.D., Lewis, M.A., MacDonald, A.M., Coleby, L.M., Talbot, J.C., Mckenzie, A.A., Bird, M.J., Cunningham J.E. and Robinson, V. (2000): The physical properties of minor aquifers in England and Wales.

British Geological Survey Technical Report, WD/00/4, Environment Agency R&D Publication 68.

Kennett, B.L.N. (2024). A Guide to the Seismic Wavefield as seen by DAS. 10.25911/ACGD-6161

Koirala, R., Kwiatek, G., Shirzaei, M., Brodsky, E., Cladouhos, T., Swyer, M and Goebel, T. (2024). Induced seismicity and surface deformation associated with long-term and abrupt geothermal operations in Blue Mountain, Nevada. Earth and Planetary Science Letters, 643, 118883, 10.1016/j.epsl.2024.118883.

Kyrkou, K., Kelly, J., Booth, A., Loveridge, F., Boon, D., Hough, E., Scott, L., Jackson, M., Butler, A., Perez, D. and Chalari, A. (2026). Insights on the heterogeneity of thermal transfer in the chalk aquifer using fibre-optic distributed temperature sensing. Geothermics, 140, 103712, 10.1016/j.geothermics.2026.103712.

Liner, C.L. (2004). Elements of 3D seismology (2nd edition). Pennwell, Tulsa, OK.

Li., Y., Ermert, L.A., Sanchez-Sesma, F.J., Escobar Maya, L.I. and Spica, Z.J. (2025). Monitoring spatio-temporal seismic velocity change using seismic interferometry and distirbuted acoustic sensing in Mexico City. Journal of Geophysical Research: Solid Earth. 130(8), e2024JB030697, 10.1029/2024JB030697.

Liu, Y., Liu, L., Jin, G., Wu, K., Reagan, M. and Moridis, G. (2023). Simulation-based evaluation of the effectiveness of fiber-optic sensing in monitoring and optimizing water circulation in next-generation enhanced geothermal systems. Geoenergy Science and Engineering, 221, 211378, 10.1016/j.geoen.2022.211378.

Loveridge, F., Holmes, G., Powrie, W. and Roberts, T. (2013). Thermal response testing through the Chalk aquifer in London, UK. Proceedings of the Institution of Civil Engineers-Geotechnical Engineering, 166(2), 197-210. 10.1680/geng.12.00037.

Mavko, G., Mukerji, T. and Dvorkin, J. (2020). The Rock Physics Handbook. Cambridge University Press, 3rd Edition. 10.1017/9781108333016.

Ouellet, S., Dettmer, J., Mikesell, T. Dylan, Lato, M., and Karrenbach, M. (2025). Tailings dam performance monitoring by combining coda wave interferometry with Distributed Acoustic Sensing. Journal of Geotechnical and Geoenvironmental Engineering, 151(6), 10.1061/JGGEFK.GTENG-13066.

Poletto, F., Biancamaria, F. and Carcione, J.M. (2018). Sensitivity of seismic properties to temperature variations in a geothermal reservoir. Geothermics, 76, 149-163, 10.1016/j.geothermics.2018.07.001.

Seib, L., Krusemark, M., Lehr, C., Ohagen, M., Pham, H., Schedel, M., Welsch, B. and Sass, I. (2025). Distributed geothermal response test on a 750 m deep borehole thermal energy storage system. Applied Thermal Engineering, 273, 126322, 10.1016/j.applthermaleng.2025.126322.

Sparrevik, P., Meland, H.J. and Park, J. (2022). Distributed fibre optic ground deformation sensing. 11th International Symposium: Field Monitoring in Geomechanics. London, UK, 4th-7th September 2022.

Spetzler, J., & Sneider, R. (2004). The Fresnel volume and transmitted waves. Geophysics 69, 653-663.

Wang, R. (1999). A simple orthonormalization method for stable and efficient computation of Green's functions. Bulletin of the Seismological Society of America, 89 (1999), 733–741. https://doi.org/10.1785/BSSA0890030733.

Waters, C.N., Aitkenhead, N., Jones, N.S. and Chisholm, J.I. (1996). Late Carboniferous stratigraphy and sedimentology of the Bradford area, and its implications for the regional geology of Northern England. Proceedings of the Yorkshire Geological Society, 51(2), 87-101.

Woodman, J., Ougier-Simonin, A., Stavrou, A., Vazaios, I., Murphy, W., Thomas, M.E. and Reeves, H.J. (2021). Laboratory experiments and grain based discrete element numerical simulations investigating the thermo-mechanical behaviour of sandstone. Geotechnical and Geological Engineering, 39, 4795-4815.

Zang, A., Oye, V., Jousset, P., Deichmann, N., Gritto, R., McGarr, A., Majer, E. and Bruhn, E. (2014). Analysis of induced seismicity of geothermal reservoirs – An overview. Geothermics, 52, 6-21, 10.1016/j.geothermics.2014.06.005.